

pubs.acs.org/JPCC Article

Charge Transport in MAPbl₃ Pellets across the Tetragonal-to-Cubic Phase Transition: The Role of Grain Boundaries from Structural, Electrical, and Optical Characterizations

G. Sombrio, Z. Zhang, A. Bonadio, L. S. de Oliveira, T. B. de Queiroz, F. F. Ferreira, A. Janotti, and J. A. Souza*



Cite This: J. Phys. Chem. C 2020, 124, 10793-10803



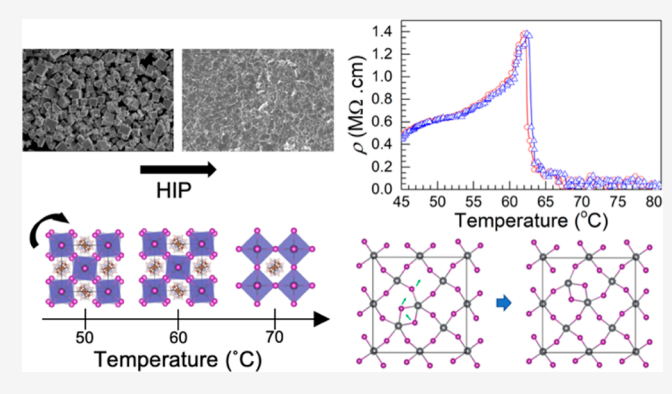
ACCESS

Metrics & More

Article Recommendations

Supporting Information

ABSTRACT: Methylammonium lead iodide (MAPbI₃) is a very promising semiconducting material for photovoltaic applications. Despite extensive research and tremendous progress, basic charge transport properties are still being debated. Combining first-principles calculations and macroscopic and local measurements, we have investigated the structural, optical, thermal, and electrical transport (ac/dc) properties of MAPbI₃ hot-pressed pellets through the tetragonal-to-cubic phase transition. Thermal analysis and X-ray diffraction experiments confirm the tetragonal-to-cubic phase change around $T_S = 56$ °C, which is often close to the working temperature of photovoltaic devices. The ac/dc electrical resistivities of the tetragonal phase indicate a metallic-like behavior as a function of temperature followed by an abrupt decrease in the



cubic phase just above T_s . In contrast to the abrupt changes observed in the electrical properties, the bandgap energy is barely affected across the phase transition. Similarly, local measurements obtained by means of nuclear magnetic resonance confirm a continuous variation in the lattice parameters and site symmetry (207 Pb and 127 I) across the structural phase transition. Density functional theory calculations combined with electrical characterizations indicate that iodine and/or unintentionally incorporated hydrogen interstitials influence decisively the charge transport activation energy in the cubic phase. In light of these findings, the unusual electrical resistivity behavior across the phase transition is discussed taking the grain boundary effects into consideration.

1. INTRODUCTION

Inorganic-organic hybrid halide perovskite crystals have been attracting considerable attention due to their excellent lightharvesting properties to convert solar energy into electricity. The power conversion efficiency in perovskite-based photovoltaic devices already exceeds 20%. 1,2 On the other hand, the charge carrier transport mechanism, along with optical properties, is still under debate, hampering improvements in the efficiency and durability of photovoltaic devices. Many research groups have focused on understanding the charge carrier transport in thin films, 3,4 single crystals,5 bulk,6 and pellets.^{7,8} Most often, the characterization of perovskite solar cells is performed in a controlled environment and at room temperature. However, in real operation conditions the solar cells are exposed to severe weather conditions, such as temperature, moisture, and ultraviolet radiation. Typically, the temperature operation of solar cells exceeds 60 °C (~343 K), 5,10 and this affects many properties of the perovskites, such as microstructure and phase segregation. In the case of methylammonium lead iodide (MAPbI₃), reports in the literature indicate the occurrence of three different structural phases as a function of temperature: orthorhombic Pnma

below -113 °C (160 K), tetragonal I4/mcm from -113 to 57 °C (160 to 330 K), and cubic $Pm\overline{3}m$ above 57 °C (330 K). Therefore, since photovoltaic device operation falls close to the tetragonal-to-cubic phase transition temperature, it is imperative to gain a better understanding of the physical properties above and below this phase transformation.

MAPbI₃ is suggested to display mixed charge carriers, meaning that electrons, holes, and ions may contribute to the electrical transport in this system.^{3,5,13} Therefore, it is crucial to investigate how charge carriers respond to external electrical fields to understand the main conduction mechanism. It has been established that the bandgap of MAPbI₃ perovskite separates the unoccupied Pb p and occupied I p bands, while the CH₃NH₃⁺ cations (MA) have negligible contribution,¹⁴

Received: January 31, 2020 Revised: April 1, 2020 Published: April 29, 2020





but their orientation may play an important role in the optical transitions. The rotation of ${\rm CH_3NH_3}^+$ can disturb the metal—halide octahedron, resulting in the direct-to-indirect bandgap, which in turn suppresses charge carrier recombination. Also, it has been suggested that the orientation of the MA cation creates ferroelectric domains in which the local electrical field assists the electron—hole separation. These properties can result in long diffusion lengths for free charges (>100 nm), long electron—hole pair lifetime (>0.1 μ s), 17 and tunable bandgap material $^{18-20}$ which are highly desirable characteristics for photovoltaic applications.

Ionic mobility in such solids involves the presence of ion vacancy or interstitial species in the crystal lattice.²¹ The activation energy of vacancy-mediated ion diffusion is determined by the vacancy formation energy (i.e., that gives the probability of finding a vacancy on a given lattice site) and the energy barrier for the vacancy migration. In the case of interstitial-mediated ion diffusion, the activation energy is given solely by the migration energy of the diffusing species. The defect formation energies reported in the literature vary over a wide range. ^{21–26} The iodine vacancy formation energy is in the range of 0-2.4 eV,²⁷ whereas iodine interstitial formation energy ranges from 0 to 1.4 eV, depending on the iodine-rich/poor limiting conditions and the position of the Fermi level in the bandgap. Between the iodine-rich and iodine-poor limits, the formation energy of the iodine interstitial is lower than that of the iodine vacancy for all positions of the Fermi level.²⁷ Reported migration barrier energies for the iodine vacancy vary from 0.17²¹ to 0.34 eV,²⁸ and for the iodine interstitial the barrier varies from 0.12²¹ to 0.33 eV²⁸ depending on the charge state of the defect and the direction along the tetragonal axis. MA and Pb vacancies were reported to have higher migration barriers, 21,28 and, therefore, are unlikely to be contributing to the ionic conductivity.

MAPbI₃ has been usually investigated as thin films, aimed at technological applications such as solar cells, light-emitting diodes, and batteries. ^{26,29–31} Herein, we report on the ac and dc electrical transport measurements of pelletized MAPbI3 across the tetragonal-to-cubic phase transition, which takes place around T_S = 56 °C. These electrical transport measurements reveal an unexpected charge transport behavior. Compared to that of the tetragonal phase, the electrical resistivity of the cubic phase decreases abruptly around the phase transition temperature, followed by a dc temperatureindependent behavior in the cubic phase region. A thermally activated transport is observed in the cubic phase, which we attribute to ionic transport. Density functional calculations are then performed to identify possible diffusing species. Note that these results differ from observations in single-crystal, films,³ and bulk, indicating that the granular microstructure plays an essential role in conductance across the grain boundaries. The analysis of the photoluminescence measurements in combination with ac and dc electrical characterizations leads to the conclusion that charge carrier transport variations across the phase transition are a bandgap independent phenomenon. While NMR data indicate no relevant contribution from the ionic (I⁻, Pb⁻, and CH₂NH₃⁺) mobility through the crystalline lattice, we note that these measurements were performed under equilibrium, i.e., not under electric field bias. Taking into account all these results, we discuss the influence of intergrain contribution on the electrical conductivity of MAPbI3 pelletized samples across the structural phase transition.

2. MATERIALS AND METHODS

2.1. Sample Preparation. Hybrid MAPbI₃ perovskites were synthesized by a simple solvothermal method at low temperatures.^{33,34} In this process, 50 mg of lead iodide is dissolved in 1 mL of hydriodic acid (45 wt % in water), and then 30 mL of isopropyl alcohol (IPA, 99.9%) is added under stirring at T_{solution} = 80 °C. Subsequently, 0.3 mL of methylamine (40 wt % in water) is added dropwise, and the final solution is stirred for 1 min. After that, the precipitated black powder is collected and washed with isopropyl alcohol twice, separated by centrifugation, and then dried in a desiccator overnight; both steps are performed at room temperature. Compacted perovskite samples (pellets) were prepared by hot isostatic pressing (HIP) at $T_{\text{synth}} = 100 \, ^{\circ}\text{C}$ under a pressure of $P = \sim 25 \text{ Pa·m}^{-2}$ for t = 5 h by using a matrix of 8 mm in diameter and 2 mm in thickness. The pellet was cut in smaller pieces with several sizes for the electrical transport measurements ranging from 3 to 8 mm. We have measured different pieces with different sizes to check the reproducibility. The geometric factor was considered in all electrical measurements. Then, gold contacts were deposited by sputtering on each side of the pellets.

2.2. Nuclear Magnetic Resonance Characterization. Nuclear magnetic resonance (NMR) spectroscopy measurements in ²⁰⁷Pb, ¹²⁷I, and ¹H were conducted in a Varian VNMRS 500 MHz spectrometer with a 4 mm narrow bore probe using an Agilent VT stack with a temperature controller. For the ²⁰⁷Pb, the resonance signal at 104.7 MHz was taken after a spin-echo pulse. The acquisition parameters were a π / 2-pulse of 3.3 μ s, interpulse delay of 20 μ s, and recycle delay of 5 s. The ²⁰⁷Pb NMR spectra were approximately 25 kHz broad, allowing us to apply a line-broadening cutoff of 2.5 kHz in the Fourier transform. The samples were encapsulated in a dried 4 mm zirconia rotor just after preparation, in order to avoid water adsorption. The experiments were performed under dried atmosphere, and by monitoring the increase of water in the ¹H NMR spectra over time, we can ensure that water adsorption has not considerably influenced the NMR results. The data are referenced to tetramethyl lead at 0 ppm using PbI₂ as a secondary reference at -25 ppm obtained at a single pulse with a magical angle spinning (MAS) of 8 kHz and temperature of 25 °C.³⁵ Approximately 1k transients were averaged to form each spectrum. The 127I NMR spectra were collected operating at a resonance frequency of 99.9 MHz. The signal was taken after a single pulse excitation. The experimental parameters were a $\pi/2$ pulse of 1 μ s and 0.5 s as a relaxation delay, using NaI as reference resonating at 225 ppm taken with MAS of 1 kHz and temperature of 25 °C. As the isotope ¹²⁷I has nuclear spin 5/2, the spectra are composed of a central transition (CT) and possibly satellite transitions (ST). Here we are concerned only with the CT, which typically has a line broadening of ~100 kHz. This spectral broadening is comfortably within the excitation pulse spectral broadening and probe sensitivity. The same statements are valid for the NMR experiments in the ²⁰⁷Pb. Approximately 2.5k transients were averaged to form each ¹²⁷I spectrum. ¹H NMR was obtained at a resonance frequency of 499.8 MHz, at MAS of 8 kHz, and using a spin-echo pulse sequence, with a $\pi/2$ of 3.4 μ s and a recycle delay of 5 s. The interpulse delay was varied from 125 ms to 2.5 s in order to measure the spinspin relaxation (T_2) of the CH₃NH₃ protons. Sixteen transients were averaged to form each ¹H spectrum.

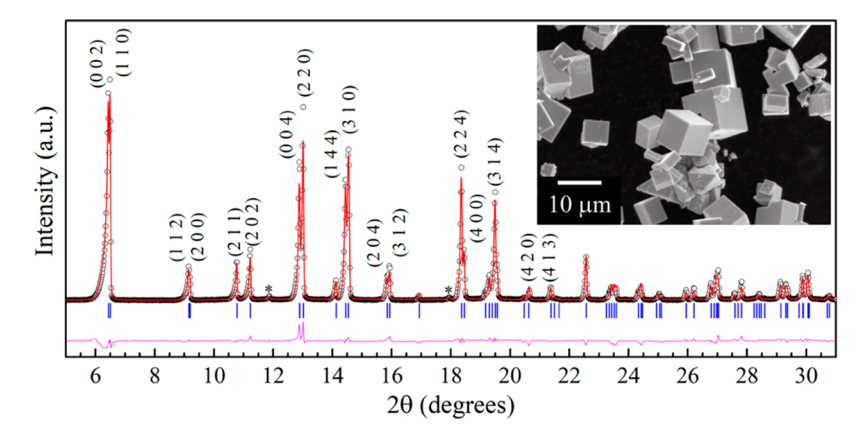


Figure 1. Room-temperature XRD Rietveld plot of the as-prepared MAPbI₃ powder synthesized by the solvothermal method, which is indexed as a tetragonal phase with *I4/mcm* space group symmetry. The difference between the experimental and simulated data is presented at the bottom. The inset exhibits an SEM image of the cuboid morphology of the as-grown samples. Asterisks indicate traces of 0.56 wt % of PbI₂.

2.3. Electrical Characterization. The electrical transport measurements were performed using a four-probe method (Keithley 2410 SourceMeter -1100 V). Impedance spectroscopy measurements were performed by using a Solartron Impedance Analyzer SI1260. All these electrical characterizations were conducted using a custom-made dedicated apparatus. Gold is evaporated on both sides of the pellet forming a thick layer with the aim to eliminate electrode effects in the impedance measurements.

2.4. X-ray Diffraction Measurements. X-ray diffraction (XRD) data were collected in a Debye-Scherrer geometry on a STADI-P diffractometer (Stoe, Darmstadt, Germany) with $MoK\alpha_1$ radiation ($\lambda = 0.7093$ Å) with a curved Ge(111)crystal, with a tube voltage of 40 kV and a current of 40 mA. Besides, XRD data from the as-grown MAPbI₃ powder and powdered pellets were collected as a function of temperature from 30 to 200 °C. The samples were hand-ground in an agate mortar and then packed into 0.5 mm quartz capillaries (Hilgenberg, Malsfeld, Germany), which were kept spinning during data collection. The Rietveld method³⁶ implemented in the GSAS software package³⁷ was used to refine the structural parameters and peak profiles from the XRD patterns. Surface morphological studies of the samples were carried out using scanning electron microscopy (SEM) (JEOL FEG-SEM JSM 6701F).

2.5. Thermal Characterization. To examine the phase transition in $CH_3NH_3PbI_3$ microcrystals, differential scanning calorimetry (DSC) was performed on a Q2000 calorimeter (TA Instruments). The experiment was conducted at a rate of 5 °C/min over a temperature range of 30–80 °C under a nitrogen atmosphere using 5 mg of sample for each run.

2.6. Optical Characterization. Photoluminescence measurements were performed as a function of temperature from 20 to 81 °C using a 488 nm (2.54 eV) line of an Ar-ion laser (MellesGriot 35 IMA 410-120) as the excitation source. The perovskite pellet was placed on a glass substrate, and the temperature was controlled by a heater. The angle of incidence was 60° measured from the normal. The PL signal from the perovskite pellet was collected by another optical fiber placed at normal incidence. The laser power was maintained at 1 mW in all measurements, and the photoemission was analyzed by a grating monochromator (Acton SP2300 with 300 groovesmm⁻¹). The signal was collected with a CCD (PIXIS 256) camera connected to the exit of the monochromator. The

diffuse reflectance spectroscopy was carried out on Varian Cary50 UV—vis spectrophotometer using a Barrelino Remote Diffuse Reflection device connected with an optical fiber coupler probe. The sample was placed on a glass substrate and irradiated with a Xenon flash lamp, and the absorption spectrum was collected from 400 to 1000 nm.

2.7. Density Functional Theory Calculations. To identify the possible sources for the ionic charge carriers, we carried out density functional theory (DFT) calculations for iodine and hydrogen interstitials. Our calculations are based on DFT^{1,2} in the generalized gradient approximation (GGA)³ as implemented in the Vienna ab initio Simulation Package (VASP) code.^{4,5} The projector augmented wave (PAW)^{6,7} method was used to describe the electron-ion interaction with a cutoff energy of 400 eV for the plane-wave basis set. We adopted the tetragonal structure for MAPbI₃ and expect that our results are also valid for the cubic structure. We first optimized the lattice parameters for the primitive cell with 4 X 4×4 *k*-points for integrations over the Brillouin zone. We then constructed a supercell, which is a $2 \times 2 \times 2$ repetition of the primitive tetragonal cell to perform the defect calculations, using a single k-point [(1/4, 1/4, 1/4)] for integrations over the Brillouin zone.

3. RESULTS AND DISCUSSION

Polycrystalline hybrid organic-inorganic MAPbI₃ perovskites were synthesized by the solvothermal method, as described above. Figure 1 shows the room-temperature XRD pattern of the as-prepared MAPbI3 powder, which was indexed to the tetragonal phase I4/mcm space group (COD ID 4124388).³⁸ This crystal structure contains ordered iodine sites at 8h positions and disordered ones at 4a positions (octahedral basal plane). The position of the organic MA molecules has been refined by using neutron diffraction data.¹¹ In our refinement, we have used those positions as fixed parameters. The unit-cell parameters, a = b = 8.850(1) Å and c = 12.637(2) Å, were obtained by Rietveld refinement and are in good agreement with the data reported in the literature. ^{39,40} The morphology of the as-grown sample is shown in the inset of Figure 1. The SEM image illustrates that the sample was synthesized as regular cuboid crystals with high size dispersity, average sizes of 7.2 μ m, and standard deviation of 1.6 μ m; see the size distribution in Figure S1 of the Supporting Information.

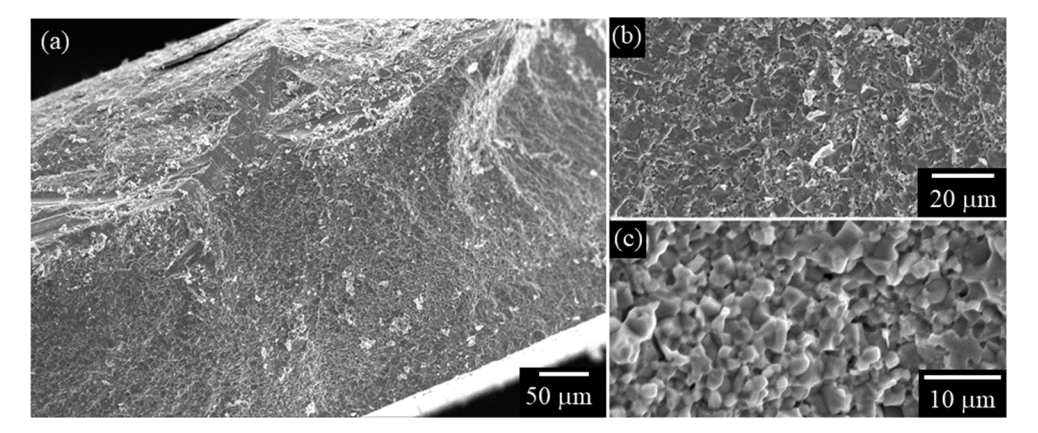


Figure 2. Cross-sectional SEM images obtained from the fractured surface of the pelletized sample of MAPbI₃ perovskite. After compression and annealing, the perovskite cuboid-shaped polycrystals turned into irregular micrograins.

The MAPbI₃ powder was compacted into pellets with simultaneous annealing at T = 100 °C for 5 h by using a hotpressure apparatus which is different from all reported works in the literature. Cross-section SEM images presented in Figure 2a-c show the fracture morphology of a pellet. The application of pressure simultaneously with temperature resulted in high-density pellets with well-defined grain boundary morphology. The fractured surface reveals a grain size of \sim 5 μ m and a very-low porosity degree. Usually, hot pressure and thermal treatment are performed in order to eliminate internal voids and porosity of the pellet sample. The combination of pressure and temperature promotes particles' growth and denser pellets. In the hybrid perovskite polycrystals, the stress caused by the HIP process deforms and compresses the cuboids resulting in a reduction of the particle size. We observe that the perovskite particles exhibit plasticity; i.e., MAPbI₃ undergoes nonreversible deformation. The perovskite particles seem to be a high-viscosity material, which results in a plastic deformation of the cuboids. The methylammonium molecule might be contributing to the highviscosity characteristics due to the interplay of the MA with the crystalline lattice.

DSC analysis was carried out to confirm the presence of the well-known structural phase transition in the MAPbI₃ pellet sample. As shown in Figure 3a, during the first heating scan, an endothermic valley was observed at $T_{\rm end}$ = 56.0 °C, revealing the temperature of the tetragonal-to-cubic phase transition. 41-43 On cooling, an exothermic peak at $T_{\rm exo} = 54.8$ °C is observed, confirming the reversibility character of this firstorder phase transition. XRD measurements as a function of temperature (see the Supporting Information) confirm the structural phase transition. Figure 3b shows the pseudocubic lattice parameters obtained by Rietveld refinements as a function of temperature, where $a_T = a/\sqrt{2}$ and $c_T = c/2$. The lattice parameters show change of about 0.4% in the tetragonal phase as the temperature increases. In the case of the tetragonal phase, the crystal structure expands along the a_T direction and decreases along the c_T direction. ⁴⁴ The Rietveld refinement for the cubic phase was performed using the space group $Pm\overline{3}m$ (COD ID 7225287)⁴⁵ where a_c is the lattice parameter of the cubic structural phase. The iodine atoms of the tetragonal phase located at the 4a site play an important role in the structural phase transition induced by temperature. The symmetry operations of this site rearrange the iodine atoms in the ab plane. As a consequence, the tilted angles are

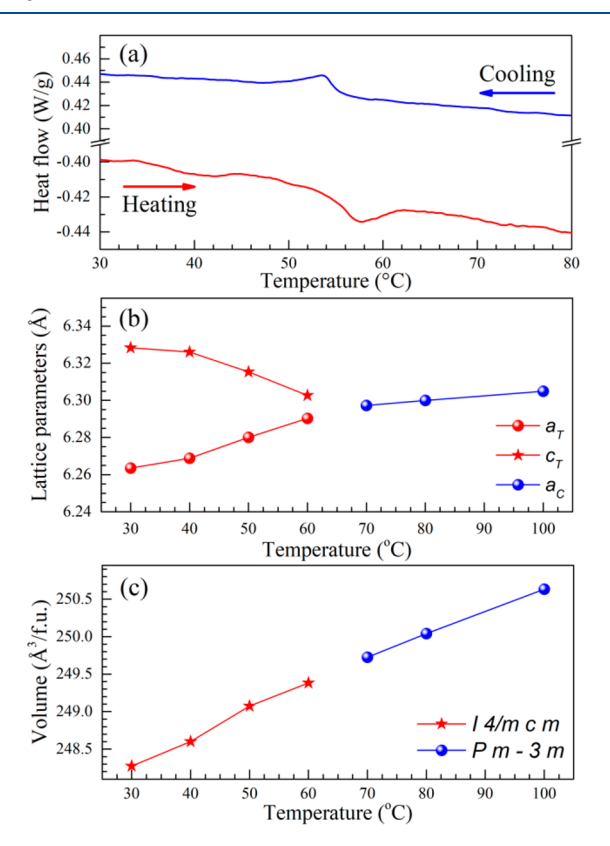


Figure 3. (a) DSC cycle of pelletized MAPbI $_3$ in the range of 30–80 °C. (b) Lattice parameters and (c) volume per formula unit as a function of temperature.

corrected by the rotation of the PbI₆ octahedral along the c_T axis, and the a_T axis expands linearly by the increase of the Pb—Pb bound distance. Also, the thermal expansion coefficient of the unit-cell volume is linear for temperatures below and above T_S , as shown in Figure 3c, indicating the harmonic effects of the crystal lattice. Atomic displacements are manifested by the shift of the (002) and (110) planes, which merge into the (100) plane of the cubic phase above the transition temperature.

Figure 4 shows the electrical resistivity of the MAPbI₃ pellet as a function of temperature. The electrical resistivity at room temperature is around 0.5 M Ω ·cm. The electrical resistivity increases with temperature until \sim 64 °C, when it reaches a maximum value of \sim 1.4 M Ω ·cm. This metallic-like behavior

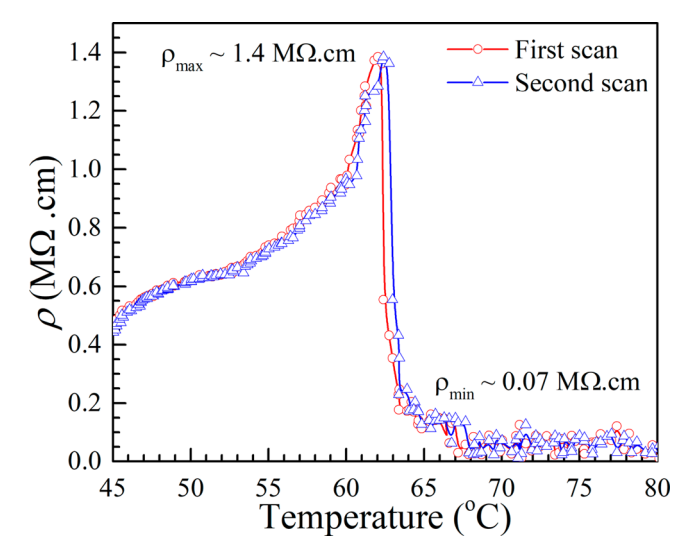


Figure 4. Electrical resistivity as a function of temperature below and above the structural phase transition.

suggests that the charge transport is influenced by the creation of vacancies as the temperature increases, which could trap the charge carriers. The trapped charge carriers are suddenly released for temperatures above $T_{\rm S}$ resulting in an abrupt drop down to ~0.07 M Ω ·cm. Then, just above the phase transition, the electrical resistivity of the cubic phase exhibits a thermally activated behavior followed by a temperature-independent behavior. Single crystals of MAPbI $_{\rm 3}$ are reported with considerably higher electrical resistivity at room temperature, about 9.5 M Ω ·cm in ref 32 and 13 M Ω ·cm in ref 47. In addition, the sudden increase in the electrical resistivity close to the phase transition is not observed in single crystals. It demonstrates that the grain boundary effects markedly influence the charge transport in such materials. 48,49

Figure 5a shows impedance spectroscopy measurements (Nyquist plot) as a function of temperature for the pelletized MAPbI₃ sample. The Nyquist plots reveal the presence of only one semicircle for each measurement. Probably, the characteristic relaxation frequencies of intragrain and intergrain contributions are close to each other, and their deconvolution is infeasible. This feature can be attributed to denser pellets due to the hot-pressure process. The electrical resistivity is defined at the low-frequency limit where the curves intercept the abscissa axis. The real component (Z') comprised of intragrain and intergrain contributions increases as a function of temperature until a maximum resistivity value of \sim 8.2 M Ω · cm, in agreement with dc measurements. Above the phase transition temperature, the electrical resistivity decreases monotonically as a function of temperature. This temperature-dependent behavior also suggests that the charge carriers are thermally activated in the cubic crystallographic phase.

Figure 5b shows the imaginary part of the impedance (Z'') as a function of frequency (f) at different temperatures in air atmosphere. All curves were normalized to a maximum of Z'' value for the sake of clarity. The characteristic relaxation frequency (f_r) of the system is defined as the maximum value of Z'' vs f. The f_r is related to the relaxation process of charge carriers or electric dipolar moments. The relaxation process is a response of the material to the temporal variation of the electric field and provides information on the charge carrier dynamics. The f_r in the tetragonal phase shifts toward lower frequencies with increasing temperature, revealing the

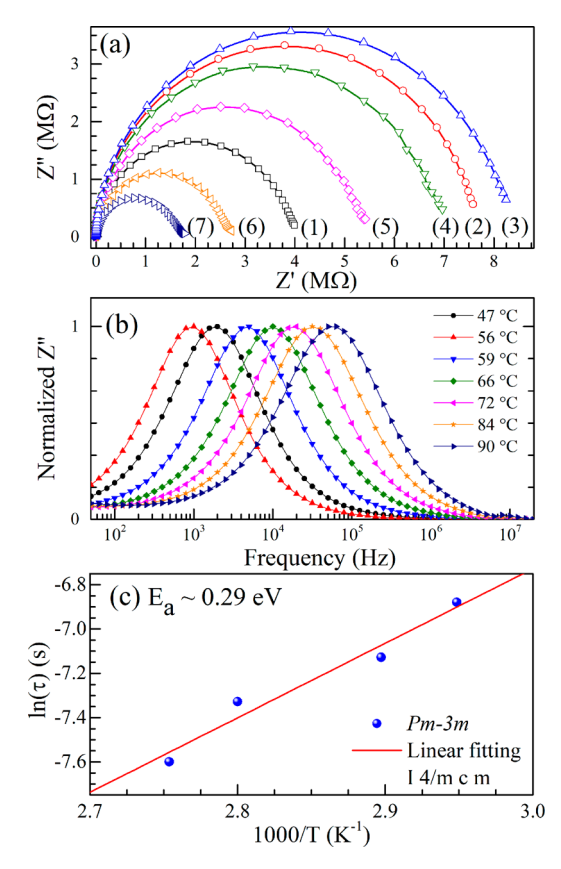


Figure 5. (a) Impedance spectroscopy measurements (Nyquist plot) for pelletized sample for several temperatures: (1) 47, (2) 56, (3) 59, (4) 66, (5) 72, (6) 84, and (7) 90 °C. (b) Normalized imaginary impedance as a function of frequency (Z'' vs f) for several temperatures. (c) Relaxation time as a function of temperature. The value of the activation energy is 0.29(5) eV.

anomalous metallic behavior also found in dc measurements. On the other hand, above the phase transition, we observe a thermally activated behavior for the relaxation time. In order to obtain the activation energy and shed light on the relaxation mechanism, relaxation time is obtained by $(\tau = 1/f_r)$. It was observed that the temperature evolution of the relaxation time obeys the Arrhenius equation, $\tau = \tau_0 \exp(-E_a/k_BT)$, where τ_0 is the pre-exponential factor, $E_{\rm a}$ is the activation energy, and $k_{\rm B}$ is the Boltzmann constant. Figure 5c shows the linear fitting performed on the $\ln(\tau)$ vs 1/T curve. The value of E_{α} obtained from the linear fitting is 0.29(5) eV. In the context of the ac electrical resistivity measurements, the activation energy can be interpreted as the energy required by the charge carriers to overcome a potential barrier for transport through the crystal lattice at temperatures above T_S . Thus, in our systems, the ac measurements suggest that the conduction is likely governed by ionic charge carriers. However, the monotonic decrease in resistivity in the ac in contrast with the dc electrical measurements may indicate that there is also an electronic contribution to the charge transport. 7,52,53

To identify the moving ionic species, we consider iodine interstitial and hydrogen impurities in DFT calculations. The former is the lowest energy defect, and the interstitial-mediated ionic migration does not involve its formation energy, rather only its migration barrier. Hydrogen, on the other hand, is a ubiquitous impurity that is present in all growth and processing environments, and it is likely to incorporate in the interstitial

sites, forming a bond with the iodine ion. We first consider the I interstitial in the 1+ and 1- charge states. The stable configurations in the two charge states are shown in Figure 6a

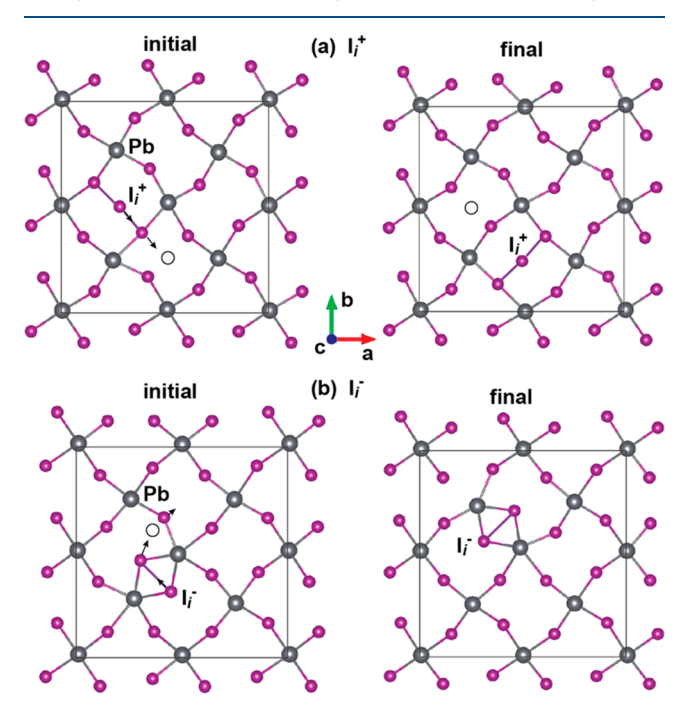


Figure 6. Configurations and migration path of I interstitial in $MaPbI_3$: (a) I_i^+ interstitial; (b) I_i^- interstitial. For the sake of clarity, only the Pb and I atoms in the ab- plane are shown.

and b. In the 1+ charge state, the iodine interstitial is closest to the two other iodine sitting at the regular lattice sites, forming a trimer. Due to the high packing density of the perovskite crystal structure, the lowest energy migration barrier involves I_i^+ kicking a neighboring iodine from its lattice site, displacing it to an interstitial site, as shown in Figure 6a.

In the 1- charge state (I_i^-) , the interstitial iodine forms an I_2 dimer structure as shown in Figure 6b. We can understand the structure of I_i as follows. An extra I atom in the MAPI crystal may approach an I sitting at a regular site, and together they form an I2 dimer sharing a regular lattice site in a so-called split interstitial configuration. The free I2 dimer is a closed-shell system. However, in MAPbI₃, the I₂ dimer occupies the site of a single I ion, which normally receives one electron from the two neighboring Pb ions. So, it is reasonable to expect that a neutral I2 replacing one I will be negatively charged, Ii-. The migration of I_i⁻ involves one of the I atoms in the I₂ dimer structure moving toward a neighboring I, forming a new dimer with it. We find a migration barrier of 0.60 eV for I_i⁺ and 0.15 eV for Ii. The latter is in good agreement with the calculated value of 0.12 eV reported by Meggiolaro et al.21 and of 0.19 eV for migration in the ab plane reported by Ming et al.²⁸ The migration barrier for Ii+ has not yet been reported in the literature to the best of our knowledge, despite it having been predicted to be a stable charge state configuration²⁸ when the Fermi level is near the valence band.

In the case of the interstitial H impurity, we find that in the positive charge state, H_i^+ , the H ion forms a bond with one lattice I. In the lowest energy configuration, H_i^+ sits in the middle of two equatorial I atoms, while it is closer to one I by 0.2 Å than to the other, as shown in Figure 7 (initial). In the first step of the H_i^+ migration, the H ion moves closer to the

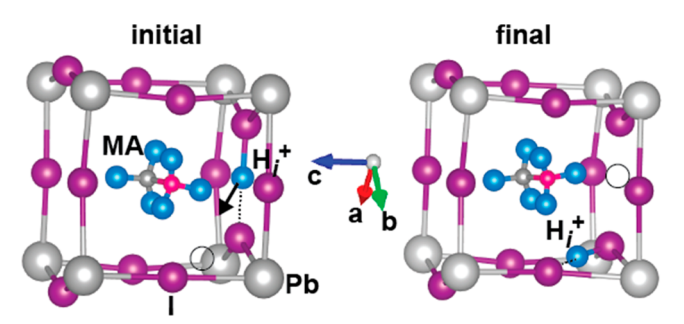


Figure 7. Most stable configuration. Migration path of the interstitial hydrogen impurity in the positive charge state, H_i^+ . Left panel: initial configuration where the H_i^+ is connecting two equatorial I; right panel: final configuration where H_i^+ is bridging an equatorial and an apical I. The a, b, and c axes of the tetragonal crystal structure are indicated.

next nearest equatorial I. This is followed by a rotation of the H ion around this equatorial I, ending close to a nearest apical I. After the last step, the H_i^+ ends up bridging an equatorial and an apical I, as shown in Figure 7 (final). This process is accompanied by a significant local structure relaxation. The calculated migration barrier is 0.3 eV, in good agreement with the reported value of 0.29 eV. In the neutral and negative charge states, $H_i^{\ 0}$ and $H_i^{\ -}$, previous calculations indicate much higher migration barriers, i.e., higher than 0.5 eV, and have not been considered here. Therefore, from the DFT calculations discussed above, we conclude that the possible species contributing to the ionic conductivity are positive interstitial hydrogen H_i^+ and negatively charged iodine interstitial I_i^- .

Ionic mobility and possible local structure variation across the phase transition were also investigated by NMR measurements. However, note that these measurements were not performed under bias. Figure 8 shows the ²⁰⁷Pb NMR spectra of the MAPbI₃ (left panel), their center of gravity, and broadening as a function of temperature (right panels). The spectra are broad lines with their center of gravity increasing in frequency from 1360 to 1420 ppm as temperature increases, while their broadening decreases linearly from 290 to 240 ppm (with some intense scattering at temperatures higher than 55 °C). The fact that the powder pattern is observed as quasisymmetric lines is related to the high symmetry of the tetragonal and cubic structures. The ^{207}Pb is an I=1/2 nuclei with a broad chemical shift range due to its large orbital extension; thus, its center of gravity is highly influenced by site symmetry and site distortions. Its spectral broadening is dominated by the chemical shift anisotropy powder pattern and dipolar coupling, i.e., site symmetry and their surrounding atoms and the bonding distances. The seemingly linear behavior of both parameters indicates that the ²⁰⁷Pb neighbors are not promoted as mobile ions, and its site symmetry changes smoothly as the temperature increases over the phase

transition (in agreement with the XRD results).

Figure 9 shows the ¹²⁷I NMR spectra of the sample as a function of temperature (left panel) and the center of gravity and broadening of the central transition resonance line (right panels). The spectra are composed of a CT resonance around -500/-1500 ppm and side peaks corresponding to ST. It is worth mentioning that due to the fast spin-spin relaxation rates (that reflect a high spectral broadening), spin-echo experiments could not be performed, but single pulse ones and the phasing of the spectra are not unambiguous. For the sake of comparison, we impose the same phasing for all the spectra

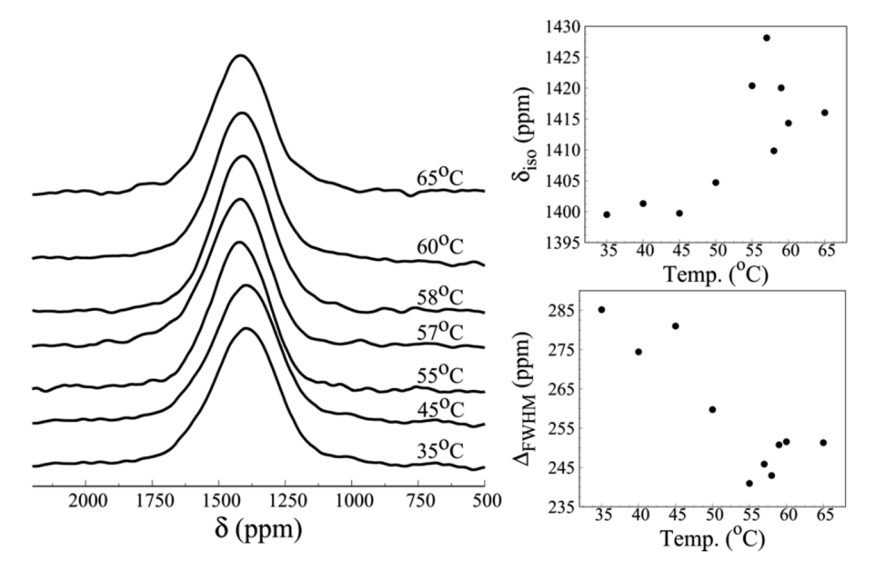


Figure 8. ²⁰⁷Pb NMR spectra of the MAPbI₃ (left panel), their center of gravity, and broadening as a function of temperature (right panels).

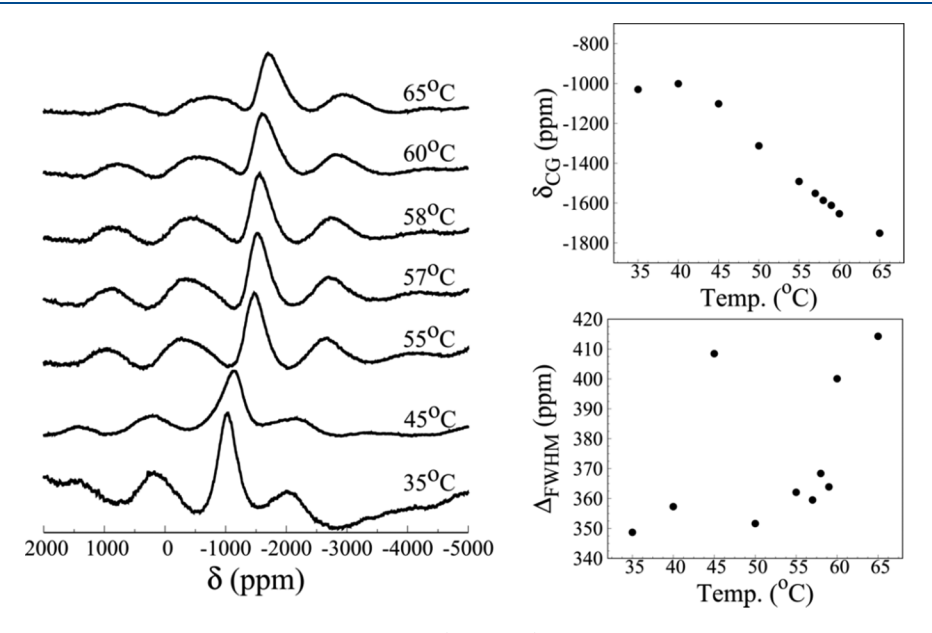


Figure 9. ¹²⁷I NMR spectra of the sample as a function of temperature (left panel) and the center of gravity and broadening of the central transition resonance line (right panel).

(by choosing the spectral shape), but that does not exclude possible distortions in the spectra (see the experimental section). However, this is the first 127 I NMR data at high magnetic field reported for the MAPbI₃, and the spectra can show site distortions and mobile ions (more commonly reported is Nuclear Quadrupolar Resonance on 127 I). The 127 I is an I = 5/2 nuclei with high quadrupole moment (-0.79×10^{28} Q/m²), such that the quadrupole coupling is the dominant effect in the spectral broadening. For that reason, the static and the MAS spectra are identical (not shown), since MAS is not capable of average second-order quadrupolar anisotropies. The spectral broadening is an evidence of small site asymmetries while the presence of mobile iodine ions is manifested as narrow resonance lines.

Figure 9 (right panel) shows that there are no systematic changes in the ¹²⁷I spectral broadening as temperature increases, but the data are scattered around 360 ppm. This fact indicates that free iodine is not being generated in the

MAPbI₃ pellets as the temperature increases over the transition phase, or, if so, it does not represent more than 5% in the relative ratio, which is our estimate for the technique detection sensitivity. Furthermore, the center of gravity of the central transition line shifts to lower frequencies as temperature increases linearly. The center of gravity is also influenced by the site symmetry, and its linear behavior evidences that the changes in the ¹²⁷I site around the phase transition temperature are a smooth process of adjustment from the tetragonal to the cubic phase, not only in terms of its crystal structure (as evidenced by the XRD data) but also locally.

We have also collected 1 H MAS NMR spin—echo spectra for the MAPbI₃ sample (see the Supporting Information for representative spectra and T_2). At short evolution times (<1.5 ms), the spectra resemble the single pulse ones. It has two peaks at 3.5 and 6.5 ppm, which are due to the 1H from the methylene and ammonium groups, respectively. These are the 1H in the CH₃NH₃ structure of the perovskite. As the

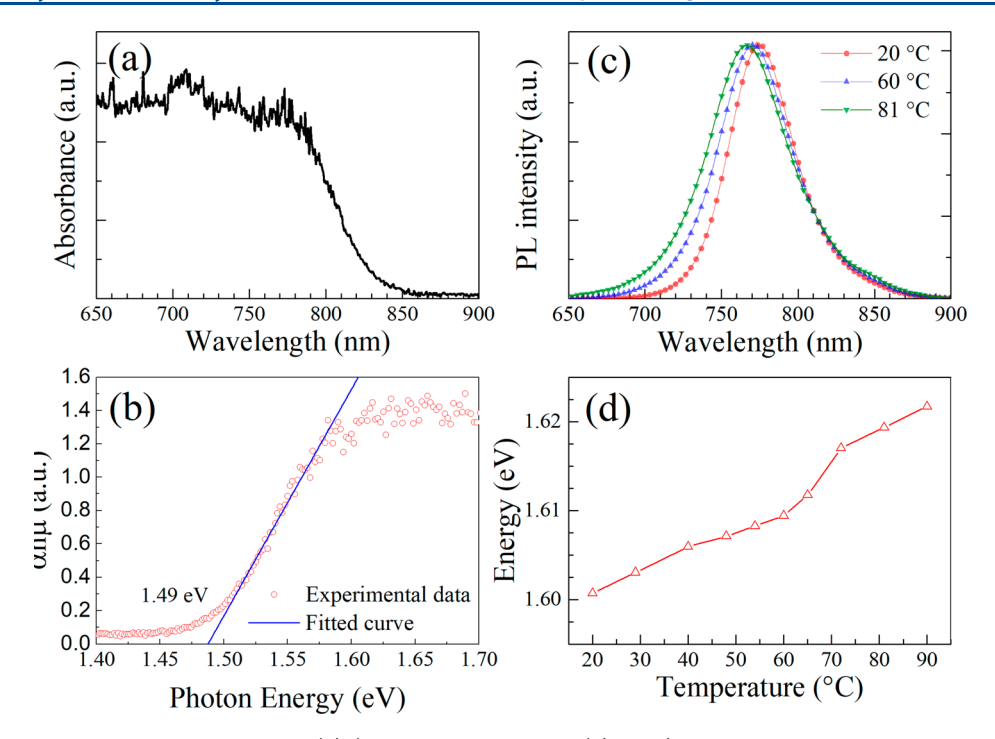


Figure 10. (a) Absorbance at room temperature and (b) (the y-axis label of figure (b) is cut) the band-to-band optical transition determined by the Tauc plot fitting from the UV-vis absorption spectra for a direct-bandgap semiconductor. The zero-crossing point gives $E_g = 1.49$ eV. (c) Photoluminescence spectra at selected temperatures of MAPbI₃ pelletized sample. (d) Energy gap variation as a function of all measured temperatures.

interpulse delays are done longer, these signals are suppressed due to the homonuclear dipolar coupling, the driving mechanism for the spin-spin relaxation in ¹H solid-state NMR for such structures. The signal suppression is more pronounced in immobile ¹H isotopes. Thus, at longer interpulse delays (~2.5 ms), the spectra are dominated by "liquidlike" ¹H isotopes. There remain three resonance signals, one more intense at 1.2 ppm and two small peaks at 3.8 and 4.7 ppm. The peak at 1.2 ppm is most likely due to small portions of adsorbed water in the sample, and the other peaks are difficult to be identified, but they represent marginal amounts of ¹H isotopes in the sample. Most importantly, there are no additional mobile protons as the temperature increases even above the tetragonal-to-cubic phase transition, since the T_2 of the signals related to the methylammonium protons remain steady for all temperatures (in agreement with the conclusions from the DFT results).

We have also investigated the temperature-dependent optical properties across the phase transition in order to gain a better understanding of the charge transport mechanism changes and the impact on the electrical resistivity. The optoelectronic properties of semiconducting materials are closely related to the bandgap and electron—hole pair creation. The transport mechanism of the intrinsic semiconducting materials is determined by the bandgap value. Besides, light emission properties also reveal information about the bandgap. The absorbance of the perovskite powder was measured by using the UV-vis spectroscopy characterization at room temperature in the wavelength region 650-900 nm; see Figure 10a. The band-to-band optical transition was determined by the Tauc plot from the UV-vis absorption spectra for a direct-bandgap semiconductor without excitonic effects (Figure 10b). The zero-crossing point gives E_{σ} = 1.49(1) eV, which is lower than the previously reported values

for both polycrystalline bandgap energy (about 1.61 eV)²⁰ and high-quality single crystals (about 1.51 eV).⁵⁵ Also, we performed PL emission measurements as a function of temperature across the phase transition. Figure 10c shows representative PL spectra at 20, 60, and 81 °C to better illustrate the effect of phase transition. Figure 10d shows the energy gap variation as a function of temperature. The PL behavior of the MAPbI₃ sample is in good agreement with the light emission from thin films, microwires, nanowires, and other irregular morphologies reported in the literature. S6-58 We have observed a slight blue-shift due to line broadening with increasing temperatures. A negligible change in the bandgap energy is observed despite the drastic decrease in the electrical resistivity from below to above $T_{\rm S}$, in agreement with other studies. S8,59

Both macroscopic and local measurements of structural, optical, thermal, and electrical transport (ac and dc) properties across the structural phase transition of pellets of MAPbI₃ have revealed important results and can be correlated as following. The XRD measurements as a function of temperature confirm the tetragonal-to-cubic phase transition of MAPbI₃ at $T_S = 56$ °C. The phase transition is accompanied by the I-Pb-I angle changing, which results in the rotation of the PbI₆ octahedral (see Figure S5 in the Supporting Information). Accordingly, ¹²⁷I and ²⁰⁷Pb NMR measurements reveal that the I and Pb sites smoothly adjust from the tetragonal to the cubic phase as temperature increases. The literature also reports that the rotation of the PbI6 octahedral is brought about by the orderdisorder of MA cations. 11,32 NMR measurements, like ¹H, ¹²⁷I, and ²⁰⁷Pb local probes, also reveal that the ionic species diffusion preserves the dynamics below and above the structural phase transition, indicating that the significant diffusion of the ionic species occurs just under the influence of an applied electrical field.

Further, the behavior of both dc and ac measurements below and above T_S is different and can shed light on the nature of the conduction mechanism. In the tetragonal phase, the resistivity increases with temperature, similarly to a metallic material for dc and ac measurements. This is in contrast to MAPbI₃ single crystals.^{7,32,60} The ac and dc measurements suggest that the conduction mechanism is governed by mixed electronic and ionic species. ^{7,52,53} Based on DFT calculations, we suggest that the activation energy of 0.29(5) eV for the ionic transport in the cubic MAPbI₃ can be explained by moving negatively charged iodine interstitials (I_i^-) or interstitial hydrogen impurities (H,+), with calculated migration energy barriers of 0.15 and 0.30 eV. The pellet of MAPbI₃ exhibits much lower electrical resistivity in comparison to single-crystalline samples, ^{32,47} suggesting a strong influence of the electric transport due to grain boundary effects. 48,49 The high electrical resistivity in the tetragonal phase can be attributed to scattering due to grain boundaries and the misalignment of the crystal lattice between neighboring grains. The abrupt decrease in resistivity with temperature across the tetragonal-to-cubic phase transition can be attributed to the isotropic nature of the cubic structure and the consequent small mismatch at the grain boundaries. Additionally, the decrease in the electrical resistivity can also be induced by intermediate energy levels, which can be created in the bandgap at the grain boundaries due to the inherent disorder (dangling bonds, defects, strain, etc.), which is a characteristic of compacted polycrystalline powder. 14,48 These intermediate energy levels can be enhanced during the phase transition due to the strong perturbation created by the mentioned intergrain effects. Indeed, both effects might be contributing to the distinguishing charge transport behavior of the pelletized MAPbI3 when going over the tetragonal-to-cubic phase transition.

4. CONCLUSIONS

We have synthesized polycrystalline MAPbI₃ powder by solvothermal methods resulting in perfect cuboid shape morphology. The hot-pressure method was used to compact the MAPbI₃ powder into low-porosity and denser pellets with well-defined grain boundary. The perovskite cuboids undergo nonreversible deformation in response to applied pressure. The MA molecule might be contributing to the plasticity of the perovskite crystals since the orientation of the MA rules the distances along the crystalline planes. Local measurements confirm the smooth variation in the crystal lattice as the temperature increases. The electrical resistivity measurements as a function of temperature reveal the metallic-like behavior in the tetragonal phase, followed by a thermal activating conduction mechanism above the tetragonal-to-cubic phase transition. Despite the drastic decrease in the electrical resistivity across the structural phase transition, a negligible change in the bandgap energy is observed through optical characterization. The ac and dc measurements demonstrate that mixed electronic and ionic species govern the conduction mechanism. DFT calculations indicate that the activation energy of 0.29 eV for the ionic transport in cubic MAPbI₃ can be explained by moving negatively charged iodine interstitials (I_i^-) or interstitial hydrogen impurities (H_i^+) . The intergrain arrangement also influences the significant difference in conductivity between the tetragonal and cubic phases, and the lattice alignment between the microstructures and the appearance of iodine surface defects or vacancies are proposed

as driving mechanisms. Overall, we have investigated the physical property nature of the tetragonal-to-cubic phase transition temperature of methylammonium lead iodide perovskite, especially concerning its charge transport and the influence of grain boundary effects in hot-pressed pelletized samples. We have shed light on the peculiar physical property nature of the tetragonal-to-cubic phase transition temperature of methylammonium lead iodide perovskite.

ASSOCIATED CONTENT

Supporting Information

The Supporting Information is available free of charge at https://pubs.acs.org/doi/10.1021/acs.jpcc.0c00887.

Experimental results of XRD and Rietveld refinements as a function of temperature; ¹H solid-state MAS NMR spectra and relaxation times; rotation angle of octahedron as a function of temperature (PDF)

AUTHOR INFORMATION

Corresponding Author

J. A. Souza — Universidade Federal do ABC, Santo André, SP, Brazil; orcid.org/0000-0002-6832-3581; Phone: +55 11995197942; Email: joseantonio.souza@ufabc.edu.br

Authors

- G. Sombrio Universidade Federal do ABC, Santo André, SP, Brazil
- Z. Zhang Department of Materials Science & Engineering, University of Delaware, Newark, Delaware 19716, United States
- A. Bonadio Universidade Federal do ABC, Santo André, SP, Brazil
- L. S. de Oliveira Universidade Federal do ABC, Santo André, SP, Brazil; o orcid.org/0000-0001-9999-206X
- T. B. de Queiroz Universidade Federal do ABC, Santo André, SP, Brazil; o orcid.org/0000-0003-3775-954X
- F. F. Ferreira Universidade Federal do ABC, Santo André, SP, Brazil; orcid.org/0000-0003-1516-1221
- A. Janotti Department of Materials Science & Engineering, University of Delaware, Newark, Delaware 19716, United

Complete contact information is available at: https://pubs.acs.org/10.1021/acs.jpcc.0c00887

Notes

The authors declare no competing financial interest.

ACKNOWLEDGMENTS

This work is supported by the Brazilian agency CNPq under grants No. 307950/2017-4, 307664/2015-5, and 404951/2016-3 and by the FAPESP under grants No. 2019/01785-8, 2017/02317-2. and 2018/15682-3. A.J. was supported by the NSF Early Career Award grant number DMR-1652994. The theroetical part of this work was supported by the XSEDE supercomputer facilities, funded by the National Science Foundation grant number ACI-1053575. The authors are grateful for Prof. Dr. Henri Ivanov Boudinov for the use of the Laboratório de Microeletrônica of the UFRGS for photoluminescence measurements. The authors are also grateful to the Multiuser Experimental Center (CEM-UFABC).

■ REFERENCES

- (1) Chen, Z.; Turedi, B.; Alsalloum, A. Y.; Yang, C.; Zheng, X.; Gereige, I.; AlSaggaf, A.; Mohammed, O. F.; Bakr, O. M. Single-Crystal MAPbI₃ Perovskite Solar Cells Exceeding 21% Power Conversion Efficiency. ACS Energy Lett. 2019, 4, 1258–1259.
- (2) Yang, W. S.; Park, B.-W.; Jung, E. H.; Jeon, N. J.; Kim, Y. C.; Lee, D. U.; Shin, S. S.; Seo, J.; Kim, E. K.; Noh, J. H.; Seok, S. I. Iodide Management in Formamidinium-Lead-Halide—Based Perovskite Layers for Efficient Solar Cells. *Science* 2017, 356 (6345), 1376—1379.
- (3) Khassaf, H.; Yadavalli, S. K.; Zhou, Y.; Padture, N. P.; Kingon, A. I. Effect of Grain Boundaries on Charge Transport in Methylammonium Lead Iodide Perovskite Thin Films. *J. Phys. Chem. C* **2019**, *123* (9), 5321–5325.
- (4) Khassaf, H.; Yadavalli, S. K.; Game, O. S.; Zhou, Y.; Padture, N. P.; Kingon, A. I. Comprehensive Elucidation of Ion Transport and Its Relation to Hysteresis in Methylammonium Lead Iodide Perovskite Thin Films. *J. Phys. Chem. C* **2019**, *123* (7), 4029–4034.
- (5) Reynolds, S.; Houghton, A. R.; Keeble, D. J. Carrier Transport in Methylammonium Lead Iodide Perovskite Single Crystals Studied by Dark Current, Steady State and Transient Photocurrent Measurements. J. Phys.: Conf. Ser. 2019, 1186, 012035.
- (6) Slonopas, A.; Foley, B. J.; Choi, J. J.; Gupta, M. C. Charge Transport in Bulk CH₃NH₃PbI₃ Perovskite. *J. Appl. Phys.* **2016**, *119* (7), 074101.
- (7) Yang, T.-Y.; Gregori, G.; Pellet, N.; Grätzel, M.; Maier, J. The Significance of Ion Conduction in a Hybrid Organic-Inorganic Lead-Iodide-Based Perovskite Photosensitizer. *Angew. Chem., Int. Ed.* **2015**, 54 (27), 7905–7910.
- (8) Almora, O.; Guerrero, A.; Garcia-Belmonte, G. Ionic Charging by Local Imbalance at Interfaces in Hybrid Lead Halide Perovskites. *Appl. Phys. Lett.* **2016**, *108* (4), 043903.
- (9) Milot, R. L.; Eperon, G. E.; Snaith, H. J.; Johnston, M. B.; Herz, L. M. Temperature-Dependent Charge-Carrier Dynamics in CH₃NH₃PbI₃ Perovskite Thin Films. *Adv. Funct. Mater.* **2015**, 25 (39), 6218–6227.
- (10) Huang, W.; Sadhu, S.; Ptasinska, S. Heat- and Gas-Induced Transformation in CH₃NH₃PbI₃ Perovskites and Its Effect on the Efficiency of Solar Cells. *Chem. Mater.* **2017**, 29 (19), 8478–8485.
- (11) Whitfield, P. S.; Herron, N.; Guise, W. E.; Page, K.; Cheng, Y. Q.; Milas, I.; Crawford, M. K. Structures, Phase Transitions and Tricritical Behavior of the Hybrid Perovskite Methyl Ammonium Lead Iodide. Sci. Rep. 2016, 6 (1), 35685.
- (12) Wright, A. D.; Verdi, C.; Milot, R. L.; Eperon, G. E.; Pérez-Osorio, M. A.; Snaith, H. J.; Giustino, F.; Johnston, M. B.; Herz, L. M. Electron-Phonon Coupling in Hybrid Lead Halide Perovskites. *Nat. Commun.* **2016**, *7* (1), 11755.
- (13) Zolfaghari, Z.; Hassanabadi, E.; Pitarch-Tena, D.; Yoon, S. J.; Shariatinia, Z.; van de Lagemaat, J.; Luther, J. M.; Mora-Seró, I. Operation Mechanism of Perovskite Quantum Dot Solar Cells Probed by Impedance Spectroscopy. ACS Energy Lett. 2019, 4 (1), 251–258.
- (14) Yin, W.-J.; Shi, T.; Yan, Y. Unusual Defect Physics in CH₃NH₃PbI₃ Perovskite Solar Cell Absorber. *Appl. Phys. Lett.* **2014**, 104 (6), 063903.
- (15) Berdiyorov, G. R.; El-Mellouhi, F.; Madjet, M. E.; Alharbi, F. H.; Rashkeev, S. N. Electronic Transport in Organometallic Perovskite CH₃NH₃PbI₃: The Role of Organic Cation Orientations. *Appl. Phys. Lett.* **2016**, *108* (5), 053901.
- (16) Xing, G.; Mathews, N.; Sun, S.; Lim, S. S.; Lam, Y. M.; Gratzel, M.; Mhaisalkar, S.; Sum, T. C. Long-Range Balanced Electron- and Hole-Transport Lengths in Organic-Inorganic CH₃NH₃PbI₃. *Science* **2013**, 342 (6156), 344–347.
- (17) Zhao, Y.; Nardes, A. M.; Zhu, K. Solid-State Mesostructured Perovskite CH₃NH₃PbI₃ Solar Cells: Charge Transport, Recombination, and Diffusion Length. *J. Phys. Chem. Lett.* **2014**, *5* (3), 490–494. (18) Ye, F.; Lin, H.; Wu, H.; Zhu, L.; Huang, Z.; Ouyang, D.; Niu, G.; Choy, W. C. H. High-Quality Cuboid CH₃NH₃PbI₃ Single Crystals for High Performance X-Ray and Photon Detectors. *Adv. Funct. Mater.* **2019**, 29 (6), 1806984.

- (19) Chen, L.; Cai, J.; Li, J.; Feng, S.-P.; Wei, G.; Li, W.-D. Nanostructured Texturing of CH₃NH₃PbI₃ Perovskite Thin Film on Flexible Substrate for Photodetector Application. *Org. Electron.* **2019**, 71, 284–289.
- (20) D'Innocenzo, V.; Srimath Kandada, A. R.; De Bastiani, M.; Gandini, M.; Petrozza, A. Tuning the Light Emission Properties by Band Gap Engineering in Hybrid Lead Halide Perovskite. *J. Am. Chem. Soc.* **2014**, *136* (51), 17730–17733.
- (21) Meggiolaro, D.; Mosconi, E.; De Angelis, F. Formation of Surface Defects Dominates Ion Migration in Lead-Halide Perovskites. *ACS Energy Lett.* **2019**, *4* (3), 779–785.
- (22) Mosconi, E.; De Angelis, F. Mobile Ions in Organohalide Perovskites: Interplay of Electronic Structure and Dynamics. *ACS Energy Lett.* **2016**, *1* (1), 182–188.
- (23) Walsh, A.; Stranks, S. D. Taking Control of Ion Transport in Halide Perovskite Solar Cells. *ACS Energy Lett.* **2018**, 3 (8), 1983–1990.
- (24) Eames, C.; Frost, J. M.; Barnes, P. R. F.; O'Regan, B. C.; Walsh, A.; Islam, M. S. Ionic Transport in Hybrid Lead Iodide Perovskite Solar Cells. *Nat. Commun.* **2015**, *6* (1), 7497.
- (25) Meloni, S.; Moehl, T.; Tress, W.; Franckevičius, M.; Saliba, M.; Lee, Y. H.; Gao, P.; Nazeeruddin, M. K.; Zakeeruddin, S. M.; Rothlisberger, U.; Graetzel, M. Ionic Polarization-Induced Current–Voltage Hysteresis in CH₃NH₃PbX₃ Perovskite Solar Cells. *Nat. Commun.* **2016**, *7* (1), 10334.
- (26) Yun, S.; Zhou, X.; Even, J.; Hagfeldt, A. Theoretical Treatment of CH₃NH₃PbI₃ Perovskite Solar Cells. *Angew. Chem., Int. Ed.* **2017**, 56 (50), 15806–15817.
- (27) Meggiolaro, D.; De Angelis, F. First-Principles Modeling of Defects in Lead Halide Perovskites: Best Practices and Open Issues. *ACS Energy Lett.* **2018**, 3 (9), 2206–2222.
- (28) Ming, W.; Chen, S.; Du, M.-H. Chemical Instability Leads to Unusual Chemical-Potential-Independent Defect Formation and Diffusion in Perovskite Solar Cell Material CH₃NH₃PbI₃. *J. Mater. Chem. A* **2016**, 4 (43), 16975–16981.
- (29) Tan, Z.-K.; Moghaddam, R. S.; Lai, M. L.; Docampo, P.; Higler, R.; Deschler, F.; Price, M.; Sadhanala, A.; Pazos, L. M.; Credgington, D.; Hanusch, F.; Bein, T.; Snaith, H. J.; Friend, R. H. Bright Light-Emitting Diodes Based on Organometal Halide Perovskite. *Nat. Nanotechnol.* **2014**, *9* (9), 687–692.
- (30) Meredith, P.; Armin, A. LED Technology Breaks Performance Barrier. *Nature* **2018**, *562* (7726), 197–198.
- (31) Xia, H.-R.; Sun, W.-T.; Peng, L.-M. Hydrothermal Synthesis of Organometal Halide Perovskites for Li-Ion Batteries. *Chem. Commun.* **2015**, *51* (72), 13787–13790.
- (32) Baikie, T.; Barrow, N. S.; Fang, Y.; Keenan, P. J.; Slater, P. R.; Piltz, R. O.; Gutmann, M.; Mhaisalkar, S. G.; White, T. J. A Combined Single Crystal Neutron/X-Ray Diffraction and Solid-State Nuclear Magnetic Resonance Study of the Hybrid Perovskites CH₃NH₃PbX₃ (X = I, Br and Cl). *J. Mater. Chem. A* **2015**, 3 (17), 9298–9307.
- (33) Semenova, O. I.; Yudanova, E. S.; Yeryukov, N. A.; Zhivodkov, Y. A.; Shamirzaev, T. S.; Maximovskiy, E. A.; Gromilov, S. A.; Troitskaia, I. B. Perovskite CH₃NH₃PbI₃ Crystals and Films. Synthesis and Characterization. *J. Cryst. Growth* **2017**, *462*, 45–49.
- (34) Guo, F.; Zhang, B.; Wang, J.; Ba, H.; Guo, R.; Huang, Y.; Ren, P. Facile Solvothermal Method to Synthesize Hybrid Perovskite CH₃NH₃PbX₃ (X = I, Br, Cl) crystals. *Opt. Mater. Express* **2017**, 7 (11), 4156.
- (35) Taylor, R. E.; Beckmann, P. A.; Bai, S.; Dybowski, C. 127 I and 207 Pb Solid-State NMR Spectroscopy and Nuclear Spin Relaxation in PbI₂: A Preliminary Study. *J. Phys. Chem. C* **2014**, *118* (17), 9143–9153.
- (36) Rietveld, H. M. A Profile Refinement Method for Nuclear and Magnetic Structures. *J. Appl. Crystallogr.* **1969**, 2 (2), 65–71.
- (37) Larson, A. C.; Dreele, R. B. V. General Structure Analysis System (GSAS); Los Alamos National Laboratory Report LAUR 86-748, 2004.

- (38) Yamada, Y.; Yamada, T.; Phuong, L. Q.; Maruyama, N.; Nishimura, H.; Wakamiya, A.; Murata, Y.; Kanemitsu, Y. Dynamic Optical Properties of CH₃NH₃PbI₃ Single Crystals As Revealed by One- and Two-Photon Excited Photoluminescence Measurements. *J. Am. Chem. Soc.* **2015**, *137* (33), 10456–10459.
- (39) Dang, Y.; Liu, Y.; Sun, Y.; Yuan, D.; Liu, X.; Lu, W.; Liu, G.; Xia, H.; Tao, X. Bulk Crystal Growth of Hybrid Perovskite Material CH₃NH₃PbI₃. CrystEngComm **2015**, 17 (3), 665–670.
- (40) Xie, J.; Liu, Y.; Liu, J.; Lei, L.; Gao, Q.; Li, J.; Yang, S. Study on the Correlations between the Structure and Photoelectric Properties of CH₃NH₃PbI₃ Perovskite Light-Harvesting Material. *J. Power Sources* **2015**, 285, 349–353.
- (41) Betancur, R.; Ramirez, D.; Montoya, J. F.; Jaramillo, F. A Calorimetric Approach to Reach High Performance Perovskite Solar Cells. Sol. Energy Mater. Sol. Cells 2016, 146, 44–50.
- (42) Ramirez, D.; Montoya, J. F.; Uribe, J. I.; Jaramillo, F. Study of the Crystallization of Metal Halide Perovskites Containing Additives via Differential Scanning Calorimetry. *J. Electron. Mater.* **2018**, 47 (10), 6319–6327.
- (43) Han, G.; Wang, F.; Jia, C.; Chen, Y.; Guan, M.; Liu, H.; Zhang, Q. Enhancement of Phase Transition Temperature from 57 to 90 °C for CH₃NH₃PbI₃ Perovskite via SnCl₂ Doping. *Mater. Chem. Phys.* **2018**, 219, 82–89.
- (44) Jacobsson, T. J.; Schwan, L. J.; Ottosson, M.; Hagfeldt, A.; Edvinsson, T. Determination of Thermal Expansion Coefficients and Locating the Temperature-Induced Phase Transition in Methylammonium Lead Perovskites Using X-Ray Diffraction. *Inorg. Chem.* **2015**, *54* (22), 10678–10685.
- (45) Luan, M.; Song, J.; Wei, X.; Chen, F.; Liu, J. Controllable Growth of Bulk Cubic-Phase CH₃NH₃PbI₃ Single Crystal with Exciting Room-Temperature Stability. *CrystEngComm* **2016**, *18*, 5257.
- (46) Maughan, A. E.; Ganose, A. M.; Candia, A. M.; Granger, J. T.; Scanlon, D. O.; Neilson, J. R. Anharmonicity and Octahedral Tilting in Hybrid Vacancy-Ordered Double Perovskites. *Chem. Mater.* **2018**, 30 (2), 472–483.
- (47) Pisoni, A.; Jaćimović, J.; Barišić, O. S.; Spina, M.; Gaál, R.; Forró, L.; Horváth, E. Ultra-Low Thermal Conductivity in Organic—Inorganic Hybrid Perovskite CH₃NH₃PbI₃. *J. Phys. Chem. Lett.* **2014**, 5 (14), 2488–2492.
- (48) Jiang, X.; Hoffman, J.; Stoumpos, C. C.; Kanatzidis, M. G.; Harel, E. Transient Sub-Band-Gap States at Grain Boundaries of CH₃NH₃PbI₃ Perovskite Act as Fast Temperature Relaxation Centers. *ACS Energy Lett.* **2019**, *4* (7), 1741–1747.
- (49) Yun, J. S.; Ho-Baillie, A.; Huang, S.; Woo, S. H.; Heo, Y.; Seidel, J.; Huang, F.; Cheng, Y.-B.; Green, M. A. Benefit of Grain Boundaries in Organic–Inorganic Halide Planar Perovskite Solar Cells. J. Phys. Chem. Lett. 2015, 6 (5), 875–880.
- (50) Ramirez, F. E. N.; Marinho, E.; Leão, C. R.; Souza, J. A. Comprehensive Theoretical and Experimental Study of Electrical Transport Mechanism on BiFeO₃ Multiferroic Nanoparticles. *J. Alloys Compd.* **2017**, 720, 47–53.
- (51) Mukherjee, A.; Basu, S.; Chakraborty, G.; Pal, M. Effect of Y-Doping on the Electrical Transport Properties of Nanocrystalline BiFeO 3. J. Appl. Phys. 2012, 112 (1), 014321.
- (52) Senocrate, A.; Moudrakovski, I.; Kim, G. Y.; Yang, T.-Y.; Gregori, G.; Grätzel, M.; Maier, J. The Nature of Ion Conduction in Methylammonium Lead Iodide: A Multimethod Approach. *Angew. Chem., Int. Ed.* **2017**, *56* (27), *7755*–7759.
- (53) Lee, H.; Gaiaschi, S.; Chapon, P.; Marronnier, A.; Lee, H.; Vanel, J.-C.; Tondelier, D.; Bourée, J.-E.; Bonnassieux, Y.; Geffroy, B. Direct Experimental Evidence of Halide Ionic Migration under Bias in CH₃NH₃PbI_{3-x}Cl_x -Based Perovskite Solar Cells Using GD-OES Analysis. *ACS Energy Lett.* **2017**, *2* (4), 943–949.
- (54) Egger, D. A.; Kronik, L.; Rappe, A. M. Theory of Hydrogen Migration in Organic-Inorganic Halide Perovskites. *Angew. Chem., Int. Ed.* **2015**, 54 (42), 12437–12441.
- (55) Saidaminov, M. I.; Abdelhady, A. L.; Murali, B.; Alarousu, E.; Burlakov, V. M.; Peng, W.; Dursun, I.; Wang, L.; He, Y.; Maculan, G.; Goriely, A.; Wu, T.; Mohammed, O. F.; Bakr, O. M. High-Quality

- Bulk Hybrid Perovskite Single Crystals within Minutes by Inverse Temperature Crystallization. *Nat. Commun.* **2015**, *6* (1), 7586.
- (56) Segovia, R.; Ding, L.; Jiang, H.; Miao, P.; Sun, X.; Shi, H.; Gao, B. Effect of Phase Transition Stress on the Photoluminescence of Perovskite CH $_3$ NH $_3$ PbI $_3$ Microwires. *J. Mater. Sci.* **2019**, *54* (7), 5331–5342.
- (57) Zhu, F.; Men, L.; Guo, Y.; Zhu, Q.; Bhattacharjee, U.; Goodwin, P. M.; Petrich, J. W.; Smith, E. A.; Vela, J. Shape Evolution and Single Particle Luminescence of Organometal Halide Perovskite Nanocrystals. *ACS Nano* **2015**, *9* (3), 2948–2959.
- (58) Yamada, Y.; Nakamura, T.; Endo, M.; Wakamiya, A.; Kanemitsu, Y. Near-Band-Edge Optical Responses of Solution-Processed Organic—Inorganic Hybrid Perovskite CH 3 NH 3 PbI 3 on Mesoporous TiO 2 Electrodes. *Appl. Phys. Express* **2014**, 7 (3), 032302.
- (59) Milot, R. L.; Eperon, G. E.; Snaith, H. J.; Johnston, M. B.; Herz, L. M. Temperature-Dependent Charge-Carrier Dynamics in CH ₃ NH ₃ PbI ₃ Perovskite Thin Films. *Adv. Funct. Mater.* **2015**, 25 (39), 6218–6227.
- (60) Zhang, H.; Lin, H.; Liang, C.; Liu, H.; Liang, J.; Zhao, Y.; Zhang, W.; Sun, M.; Xiao, W.; Li, H.; Polizzi, S.; Li, D.; Zhang, F.; He, Z.; Choy, W. C. H. Organic-Inorganic Perovskite Light-Emitting Electrochemical Cells with a Large Capacitance. *Adv. Funct. Mater.* **2015**, 25 (46), 7226–7232.